Check for updates

Geophysical Research Letters

RESEARCH LETTER
10.1029/2021GL096216

Increasing Winter Ocean-to-Ice Heat Flux in the Beaufort Gyre Region, Arctic Ocean Over 2006–2018

Wenli Zhong[1], Sylvia T. Cole[2], Jinlun Zhang[3], Ruibo Lei[4], and Michael Steele[3]

[1]Frontier Science Center for Deep Ocean Multispheres and Earth System (FDOMES) and Physical Oceanography Laboratory, Ocean University of China and Qingdao National Laboratory for Marine Science and Technology, Qingdao, China, [2]Woods Hole Oceanographic Institution, Woods Hole, MA, USA, [3]Applied Physics Laboratory, Polar Science Center, University of Washington, Seattle, WA, USA, [4]Key Laboratory for Polar Science of MNR, Polar Research Institute of China, Shanghai, China

Key Points:

- The winter ocean-to-ice heat flux increased by 0.87 ± 0.09 W/m^2 from 2006–2012 to 2013–2018 in the Beaufort Gyre region
- 2013–2018, compared with 2006–2012, had stronger convection associated with thinner ice, and increased ice mobility and lead fraction
- Changes to Ekman upwelling had a secondary role in enhanced heat flux and entrainment of subsurface heat

Supporting Information:

Supporting Information may be found in the online version of this article.

Correspondence to:

W. Zhong,
wlzhongouc@ouc.edu.cn

Citation:

Zhong, W., Cole, S. T., Zhang, J., Lei, R., & Steele, M. (2022). Increasing winter ocean-to-ice heat flux in the Beaufort Gyre region, Arctic Ocean over 2006–2018. *Geophysical Research Letters*, *49*, e2021GL096216. https://doi.org/10.1029/2021GL096216

Received 20 SEP 2021
Accepted 8 JAN 2022

© 2022. The Authors.
This is an open access article under the terms of the Creative Commons Attribution-NonCommercial-NoDerivs License, which permits use and distribution in any medium, provided the original work is properly cited, the use is non-commercial and no modifications or adaptations are made.

Abstract Ocean-to-ice heat flux (OHF) is important in regulating the variability of sea ice mass balance. Using surface drifting buoy observations, we show that during winter in the Arctic Ocean's Beaufort Gyre region, OHF increased from 0.76 ± 0.05 W/m^2 over 2006–2012 to 1.63 ± 0.08 W/m^2 over 2013–2018. We find that this is a result of thinner and less-compact sea ice that promotes enhanced winter ice growth, stronger ocean vertical convection, and subsurface heat entrainment. In contrast, Ekman upwelling declined over the study period, suggesting it had a secondary contribution to OHF changes. The enhanced ice growth creates a cooler, saltier, and deeper ocean surface mixed layer. In addition, the enhanced vertical temperature gradient near the mixed layer base in later years favors stronger entrainment of subsurface heat. OHF and its increase during 2006–2018 were not geographically uniform, with hot spots found in an upwelling region where ice was most seasonally variable.

Plain Language Summary Heat transferred from the ocean to the sea ice influences the extent to which sea ice melts or freezes. It is unclear how variable this heat transfer is during winter. Using multiple drifting instruments, our results reveal that ocean-to-ice heat transfer almost doubled from 2006–2012 to 2013–2018. The enhanced heat transfer is a result of thinner and looser sea ice that leads to enhanced ice growth during winter. This enhanced ice growth causes stronger mixing within the ocean and so larger transfers of heat from the ocean to the ice. Changes in the extent to which water is physically pushed upwards had a secondary role in enhanced ocean-to-ice heat transfer over the study period. As a result of the increased ice growth, the pool of water directly in contact with the ice cover is cooler, saltier, and deeper over 2013–2018 compared with 2006–2012. Changes in ocean temperature at depth additionally favor stronger subsurface heat entrainment during 2013–2018. Ocean-to-ice heat transfer and its increase during 2006–2018 was not geographically uniform, with hot spots found where ice was most seasonally variable.

1. Introduction

The ocean-to-ice heat flux (hereafter OHF) plays a vital role in the sea ice mass balance (e.g., Krishfield & Perovich, 2005; Maykut, 1982; Maykut & McPhee, 1995; McPhee et al., 2003). Theoretical estimates have indicated that an annual average OHF of 2 W/m^2 is needed to maintain an equilibrium ice thickness of ~3 m (Maykut, 1982; Maykut & Untersteiner, 1971). Further, OHF has a significant seasonal cycle with maximum values reaching 40–60 W/m^2 in summer (Maykut & McPhee, 1995) and generally <2 W/m^2 in winter (Krishfield & Perovich, 2005). In fact, the winter OHF is close to zero in many instances (e.g., Maykut & McPhee, 1995; McPhee et al., 2003), although with significant regional variability (Krishfield & Perovich, 2005; Lei et al., 2018). The western Arctic Ocean is dominated by first-year sea ice in recent years (Krishfield et al., 2014; Kwok, 2018; Kwok & Rothrock, 2009; Zhang et al., 2012), which leads to an increasingly important role for ice-ocean thermodynamics in determining the sea ice mass balance (Planck et al., 2020).

In summer, solar heating of the ocean surface mixed layer is the main source for OHF (Krishfield & Perovich, 2005; Maykut, 1982; Maykut & McPhee, 1995; Steele et al., 2010; Timmermans, 2015; Toole et al., 2010). In contrast, winter OHF depends strongly on entrainment of subsurface heat from the near surface temperature maximum water (NSTM), Pacific Summer Water (PSW), or Atlantic Water (AW; Fer et al., 2017; Jackson et al., 2012; Steele & Morison, 1993; Yang et al., 2001). Winter heat entrainment is influenced by the strength of halocline

stratification just below the surface mixed layer, the strength of surface convection, the momentum flux to the ocean (represented in terms of ice-ocean stresses, e.g., McPhee, 1992), the availability of subsurface heat, and potentially the tendency for Ekman upwelling in winter. All of these factors are changing interannually, creating a potential for significant changes to wintertime OHF.

1. Halocline stratification. With the weakening of the Eurasian Basin halocline, winter OHF has increased significantly via entrainment of AW heat into the mixed layer (Polyakov et al., 2020). In contrast, the Canada Basin exhibits no interannual trend of vertical mixing in the interior (Guthrie et al., 2013), likely a result of strong upper-ocean stratification that inhibits vertical mixing in general (Guthrie & Morison, 2021; Lincoln et al., 2016). In this area, subsurface heat is largely isolated from the surface mixed layer and thus rarely contributes to OHF, with the exception of sporadic storm-induced mixing events (e.g., Jackson et al., 2012; Yang et al., 2001)
2. Surface convection. Previous studies revealed that brine-driven surface convection could entrain the Atlantic Water heat upwards in the Eurasian Basin (Polyakov et al., 2013, 2020), while the strong stratification and potential lateral mixed layer restratification impede this convection process in the Canada Basin (Toole et al., 2010). Seasonally, brine-driven surface convection contributes to the entrainment of heat from the NSTM each fall (e.g., Timmermans, 2015). Further, a recent study of Cole and Stadler (2019) revealed an interesting deepening and salinification of the winter mixed layer in the Canada Basin over 2006–2017, forced by freshwater distribution changes. These changes will likely affect the entrainment of subsurface heat, and thus wintertime OHF. Whether the strength of ocean convection has changed or not is not clear
3. Momentum flux. The ice-ocean shear can drive entrainment of subsurface heat upward and thus contribute to enhanced OHF (e.g., Krishfield & Perovich, 2005; Timmermans, 2015). Using a parameterized mixed layer temperature above freezing (no interannual variations), Krishfield & Perovich (2005) revealed a positive trend of OHF over 1979–2002 due to enhanced ice drift which highlights a greater role for shear entrainment
4. Subsurface heat. Alongside changes in upper-ocean stratification, the NSTM is becoming warmer as ice is becoming thinner in the Canada Basin (e.g., Jackson et al., 2010, 2012; Steele et al., 2011; Timmermans, 2015). In addition, the heat content of the interior Beaufort Gyre halocline layer has doubled over the past 30 years in the Canada Basin (Timmermans et al., 2018). It is unclear how wintertime heat entrainment is influenced by these warmer subsurface waters interannually
5. Ekman upwelling. Heat entrainment may also be influenced by Ekman pumping, with upwelling conditions more likely to result in entrainment. Recent studies have shown a large area of upwelling in the southern Canada Basin in winter (Dewey et al., 2018; Meneghello et al., 2018; Zhong et al., 2018; also see Figure 1) that results from including the recently nonnegligible surface geostrophic current in the calculation of Ekman pumping (downwelling would be estimated if geostrophic currents are neglected). While the effects of this upwelling region on OHF is yet to be determined, it has the potential to be the primary area for wintertime OHF

To address the potential spatial and interannual variability of wintertime OHF, we examine the changes to OHF and the mechanisms that control it over 2006–2018 using both observations and a numerical model. To the best of our knowledge, this is the first comprehensive study to investigate winter OHF over such a long-time scale and the basin wide Beaufort Gyre region. The data and methods we used are described in Section 2. Estimates of OHF considering the surface geostrophic current are presented in Section 3.1. In Section 3.2, we evaluate the entrainment of subsurface heat into the mixed layer and its impacts on OHF. The proposed mechanism for enhanced OHF is described in Section 3.3. Conclusions and discussion are presented in Section 4.

2. Data and Methods

For OHF, we consider the months of January-March only, thus excluding the effect of solar radiation on the mixed layer. During these months, <0.02 W/m^2 of solar radiation could penetrate to the bottom of sea ice in our study region (not shown). This is negligibly small compared with our considered OHF. January-March is a time when sea ice formation and vertical ocean convection (brine rejection) dominate, and when sea ice properties are likely most uniform spatially and perhaps interannually (e.g., Brenner et al., 2021). This is also the season when upwelling dominates in the southern Beaufort Gyre region (Figure 1, also see Meneghello et al., 2018; Zhong et al., 2018).

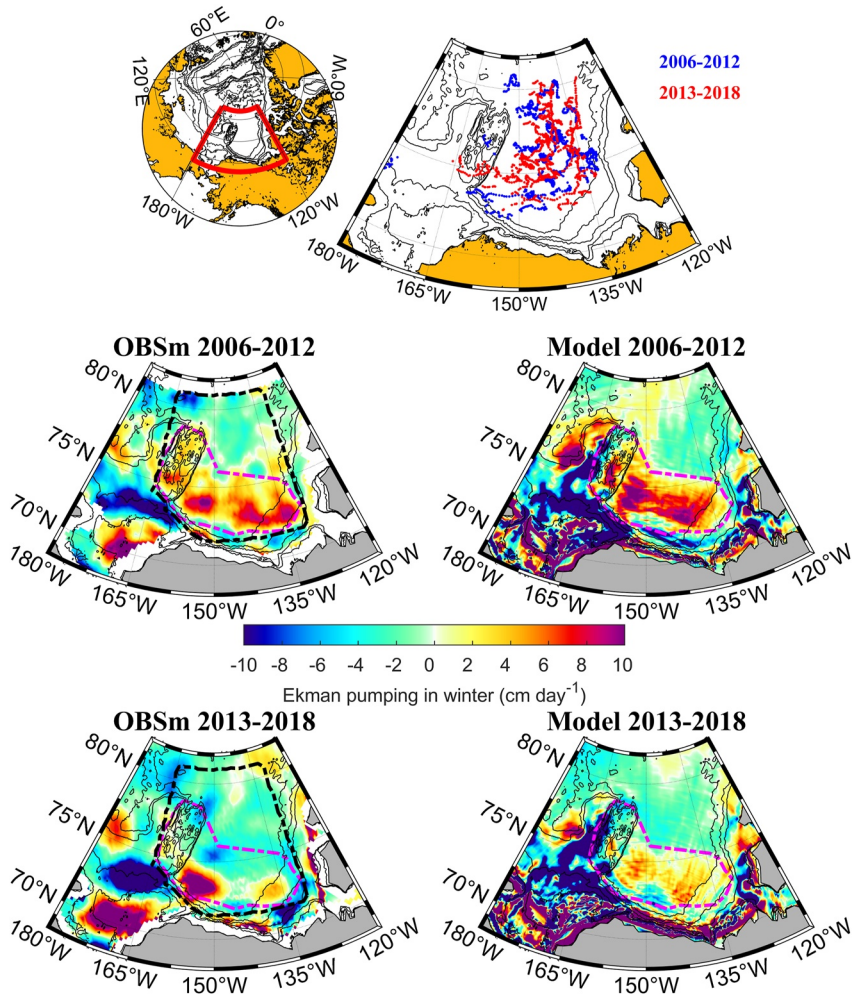

Figure 1. Ekman pumping in winter (January-March) in two periods (2006–2012, 2013–2018) from the observational method (OBSm) and Marginal Ice Zone Modeling and Assimilation System (MIZMAS) model. The dashed pink line in the middle and bottom panels represents the defined upwelling region while the dashed black line represents the defined Beaufort Gyre region (hereinafter BG region). The Ice-Tethered Profiler (ITP) and Autonomous Ocean Flux Buoy (AOFB) drift trajectories in winter in the two periods are shown in the top panel.

Ice-Tethered Profiler (ITP, fully processed level 3 data) and Autonomous Ocean Flux Buoy (AOFB, flux package data) observations from January 2006 to March 2018 are used to estimate OHF. The details of ITP and AOFB records that we used are provided in Table S1 in Supporting Information S1. The ITPs measure the ocean pressure, temperature, and salinity between ~7 and ~750 m with sensor accuracies of ±1 dbar, ±0.001 °C, ±0.005, respectively; detailed data processing procedures can be found at http://www.whoi.edu/itp (Krishfield et al., 2008). For AOFB data, the measured temperature (±0.001 °C) and conductivity (±0.002 mS cm^{-1}) at 7.6 m below the surface of the ice are used (Shaw et al., 2008). Detailed data processing procedures are referred to https://www.oc.nps.edu/~stanton/fluxbuoy/index.html. The daily mean buoy data are used to calculate the parameterized OHF, which minimizes the impact of inertial currents.

In this study, we are interested in the ocean-to-ice heat flux from a large-scale perspective and so employ a parameterized method since direct turbulent measurements are rare and sparse both in space and time. The parameterized OHF is calculated as $OHF = \rho_{ocean} c_p u_* C_H (T_{7m} - T_f)$, where $\rho_{ocean} = 1023\ \ kg\ \ m^{-3}$ is a reference mixed layer density, $c_p = 3980$ J/(°C kg) is the specific heat of seawater, T_{7m} and T_f are the mixed layer temperature and freezing point at the depth of ~7 m, respectively, and $C_H = 0.0057$ is the heat transfer coefficient (McPhee, 1992; McPhee et al., 2003). T_{7m} and T_f are derived from measurements at the shallowest depth of ITPs and AOFBs which is usually at a depth of 6–7 m (within the winter mixed layer depth). In winter, $T_{7m} - T_f$ is very small

(with an accuracy of 0.001 °C). T_f is controlled by the variability of salinity while T_{7m} is influenced by the heat conduction through the ice to the atmosphere, heat entrainment from subsurface warm water and the lateral heat advection. The friction velocity $u_* = \sqrt{|\tau_{ice-ocean}|/\rho_{ocean}}$ (Maykut & McPhee, 1995) is determined by a parameterized ice-ocean stress $\tau_{ice-ocean} = \rho_{ocean} C_{io} |(\vec{u}_{ice} - \vec{u}_{ocean})| R_o(\vec{u}_{ice} - \vec{u}_{ocean})$ (e.g., Hibler, 1979; Hibler & Bryan, 1987) where the ice-ocean drag coefficient C_{io} is taken to be 0.0055 and R_o is a rotation matrix for the ocean (McPhee, 1975). The turning angle $\theta = 25^o$ is used for the geostrophic current $\vec{u}_{\text{ocean}}$, as the turning angle usually lies in the range $20° < \theta < 30°$ (McPhee, 1975). The ice velocities are derived from the buoys' drifting positions while the surface geostrophic current is derived from the satellite observation (Text S2 in Supporting Information S1). Using the ice-ocean drag law to derive friction velocity instead of direct measurement (McPhee, 1992) results in a change of only 10–20% in OHF (Steele & Morison, 1993). The uncertainty of parameterized OHF compared with the direct turbulent measurement is also discussed in Peterson et al. (2017). Potential uncertainties due to interannual or spatial variability resulting from differing properties of the sea ice cover are discussed in Section 4.

The Ekman pumping velocity that takes into account the surface geostrophic current is calculated according to the methods presented in Zhong et al. (2018) using both observations and model results (also see Text S2 in Supporting Information S1 for further details). The mixed layer heat balance is governed by the following equation:

$$\rho c_p h \partial T/\partial t = \underbrace{Q_{net}}_{\text{diagnosed from the model}} - \underbrace{\rho c_p h \vec{u} \cdot \nabla T}_{\text{negligibly small}} - \underbrace{\rho c_p w_e (T_{ml} - T_d)}_{\text{diagnosed from buoy observation divided into two terms as described below}}$$

where h is the mixed layer depth, Q_{net} is the ocean surface net heat flux (the penetrative solar radiation through the mixed layer base could be neglected), $\rho c_p h \vec{u} \cdot \nabla T$ is the heat advection (for our case, it is a small term compared with others), and the last term is the entrainment heat flux (Stevenson & Niiler, 1983). $T_{ml} - T_d$ is the temperature difference between the average mixed layer temperature (T_{ml}) and the temperature just below the mixed layer base (T_d, at the depth of ~1 m below the mixed layer base), and the entrainment velocity is $w_e = H(\partial h/\partial t + w_{-h} + \vec{u} \cdot \nabla h)$, where the Heaviside unit function is used such that $H(x) = (1, x \geq 0 \ \ and \ \ 0, x < 0)$. w_{-h} is the vertical velocity at the base of mixed layer which is approximated by the Ekman upwelling here and $\vec{u}$ is the mixed layer averaged horizontal velocity. Thus, we can divide the entrainment velocity into two terms, i.e., the deepening of mixed layer depth induced entrainment velocity (which we only consider as the convective entrainment velocity) and the Ekman upwelling induced entrainment velocity. The seasonal deepening rate of the mixed layer is evaluated from the spatially averaged summer (July-October) to winter hydrographic data and then used to evaluate the convective entrainment heat flux. The mixed layer depth is defined with a threshold criterion of $\Delta\sigma = 0.1$ kg/m^3 (Peralta-Ferriz & Woodgate, 2015), where it is the potential density difference in depth from the shallowest measured depth for ITP records (note that AOFB does not allow for this analysis). The calculated daily Ekman pumping velocities are linearly interpolated to the buoys' daily mean positions.

In addition to observations, model results (ice thickness, ice velocity, ice concentration, ice growth/melt rate, and ocean surface net heat flux) from the Marginal Ice Zone Modeling and Assimilation System (MIZMAS; Zhang et al., 2016) are used to investigate the effect of changing sea ice properties on OHF and the ocean mixed layer properties. The details of the model and validation of simulated sea ice properties against observations can be found in Zhang et al. (2012, 2015, 2016, 2021a), and are presented in Text S1 and Figures S1 and S2 in Supporting Information S1.

3. Results

3.1. Winter Ocean-to-Ice Heat Flux Variability

The winter OHF was spatially and interannually variable (Figures 2a and 2b). The upwelling region in the southern Beaufort Gyre region corresponded to higher OHF than the northern region. The winter OHF increased with a rate of 0.024 ± 0.022 W/m^2 per winter month during 2006–2018 (Figure 2b). Beaufort Gyre region median values were smaller than 0.3 W/m^2 prior to 2009, and larger afterward with three maxima appearing in years 2010, 2013, and 2016 (Figure 2b). For practical and comparative reasons, we choose to consider two time periods, 2006–2012 and 2013–2018, as in Cole and Stadler (2019). These time periods approximately divide the record in half and correspond to when a significant deepening of winter mixed layer depth has been documented (Cole

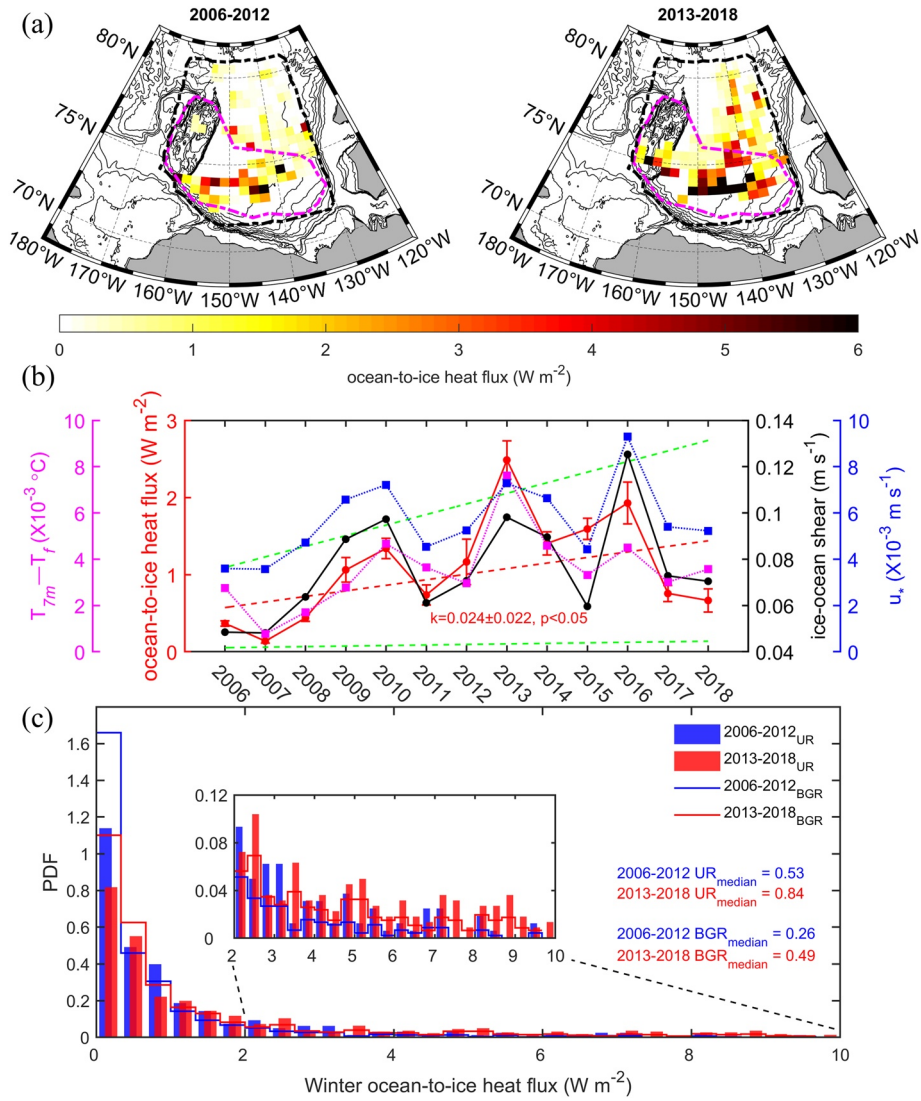

Figure 2. Statistics of winter ocean-to-ice heat flux. (a) Gridded average ocean-to-ice heat flux during 2006–2012 and 2013–2018. The original values are spatially averaged into bins of 2° in longitude and 0.5° in latitude. (b) Beaufort Gyre (BG) region mean ocean-to-ice heat flux and the standard error (error bars). In order to reduce clutter, only the median values of ice-ocean shear and the two components in the parameterized heat flux calculation ($T_{7m} - T_f$ and u_*) are shown. The dashed red line represents the linear regression fit of monthly ocean-to-ice heat flux (OHF) with 95% confidence interval (dash green lines). (c) Probability density functions (PDFs) of ocean-to-ice heat flux in the upwelling region (UR, bars) versus BG region (BGR, lines; regions defined in Figure 1) in the two time periods with median values shown in color. The inset panel shows the PDF plotted on the heat flux range of 2–10 W/m^2.

& Stadler, 2019). Here, we will look into details of the corresponding OHF, the mixed layer properties, and the Ekman pumping in these two periods. Heat fluxes larger than 5 W/m^2 were more prevalent in later period (Figure 2c), with BG region mean values that increased from 0.76 ± 0.05 W/m^2 (the uncertainty is the standard error) over 2006–2012 to 1.63 ± 0.08 W/m^2 over 2013–2018 (Figure 2b). The statistical significance of the daily heat flux difference in the two periods is evaluated using Welch's *t*-test which is statistically significant above the 99% confidence level (not shown). Variations in both $T_{7m} - T_f$ and u_* (a reflection of ice-ocean shear entrainment) contributed to the interannual variations in heat flux. Spatially, both $T_{7m} - T_f$ and u_* were elevated in the BG region especially in the upwelling region. Interannually, $T_{7m} - T_f$ increased from a median value of 1.9×10^{-3} °C to 4.5×10^{-3} °C, while u_* increased by a proportionally smaller amount from 4.8×10^{-3} to 5.8×10^{-3} m/s, suggesting that $T_{7m} - T_f$ plays a more important role than the shear entrainment (u_*) in regulating the interannual

variability of OHF over 2006–2018 (see also Figure S3 in Supporting Information S1). In the next section, we analyze the influencing factors for the increased $T_{7m} - T_f$.

3.2. Entrainment of Subsurface Heat Into the Mixed Layer

Does the upwelling in winter contribute to the large-scale changes of OHF seen in Figure 2? To explore this question, we first investigate winter Ekman pumping over 2006–2012 and 2013–2018 (Figure 1). A large area of upwelling in winter in the southern Beaufort Gyre region was evident and spatially consistent between the observations and model. This upwelling region results from ocean geostrophic currents that are large enough to drive the sea ice in winter (Dewey et al., 2018; Meneghello et al., 2018; Zhong et al., 2018). Upwelling was weaker during 2013–2018 (-0.2 ± 0.3 cm/day) relative to 2006–2012 (3.3 ± 0.1 cm/day, Figure 1), owing to changes in the velocity difference between the ice and ocean as well as changes in the spatial gradient of ice-ocean stress (Zhong et al., 2018). Thinner and less-compact sea ice in the later period would also reduce the magnitude of upwelling (Meneghello et al., 2020; Wang et al., 2019). The reduced upwelling (also divergence) would favor freshwater accumulation in the gyre center. On the other hand, thinner and less-compact sea ice potentially promotes stronger ice growth and more salt production (Petty et al., 2018). We will discuss the net effect of these processes in Section 3.3.

We next examine the average heat content within the mixed layer, which is larger in the later period especially in the upwelling region (Figure 3a). Note that the mixed layer heat content is normalized by the mixed layer depth to account for the deepening of the winter mixed layer in later years. The average mixed layer temperature was cooler in the later period (Figure 3c) due to more saline mixed layer water (e.g., middle panel of Figure 3e, or Figure 7 of Cole and Stadler (2019)). Average heat content within the mixed layer is especially sensitive to the larger values of $T - T_f$ near the base of mixed layer (Figure 3d), which were up to 10 times larger than those shallower in the mixed layer. The PDF of the variables shown in Figures 3a–3d reveals distinguishable differences between periods (Figure S4 in Supporting Information S1). The warmer temperatures (relative to T_f) at the mixed layer base are consistent with increasing heat entrained upward in recent years.

The buoy drift positions where upwelling is present are used to calculate the corresponding upwelling induced entrainment heat flux (Figure 3b). Comparing Figure 3b with Figure 2a, we can see that upwelling induced entrainment heat flux accounts for some part of OHF (also see Figures 2b and 3f). By examining their ratio, upwelling induced entrainment heat flux is usually smaller than OHF (not shown). There is no clear interannual trend of the Ekman upwelling (Figure 3f, black dashed line), and the variation of $T_{ml} - T_d$ is actually dominating the estimated entrainment heat flux with a correlation coefficient of -0.8 ($P < 0.01$; Figure 3f, pink solid line). Examining the Ekman pumping variability over all the daily mean buoy positions, the upwelling was actually weaker in later years (Figure 3f, black solid line, similar to the results in Figure 1). Even though upwelling has been weaker in later years, upwelling induced entrainment heat flux was actually larger due to the enhanced vertical temperature gradient near the mixed layer base (indicated by the increase of $T_{ml} - T_d$). The result is not sensitive to the criteria used to define mixed layer depth.

We note that upwelling is only responsible for part of the entrainment velocity. Another major part comes from the deepening of mixed layer with time (dh/dt). The mixed layer depth changes from summer values of 9.64 ± 0.52 m (2005–2011) and 14.71 ± 1.32 m (2012–2017), to winter values of 25.78 ± 0.35 m (2006–2012) and 35.42 ± 0.28 m (2013–2018), which are derived from both summer and winter hydrographic data (Figure S5 in Supporting Information S1) in the upwelling region (note the shift of years between seasons for this comparison). This suggests a stronger vertical convective entrainment and potentially wind-driven deepening due to delayed freeze-up. A rough estimation considering the summer to winter mixed layer deepening rate over 3 months would be 17.9 ± 0.6 cm/day during 2006–2012 and 23.0 ± 1.3 cm/day during 2013–2018. This corresponds to convective entrainment heat flux that increased from 0.51 ± 0.05 W/m^2 over 2006–2012 to 1.64 ± 0.06 W/m^2 over 2013–2018 (multiplied by $T_{ml} - T_d$ in Figure 3f and applied the equation of entrainment heat flux). Similar increase of convective entrainment heat flux can be achieved outside the upwelling region. With the enhanced vertical temperature gradient near the mixed layer base (e.g., Figure 3e, left panel and Figure 3f, $T_{ml} - T_d$), it is expected that an enhanced vertical heat flux would take place and thus the increase of OHF.

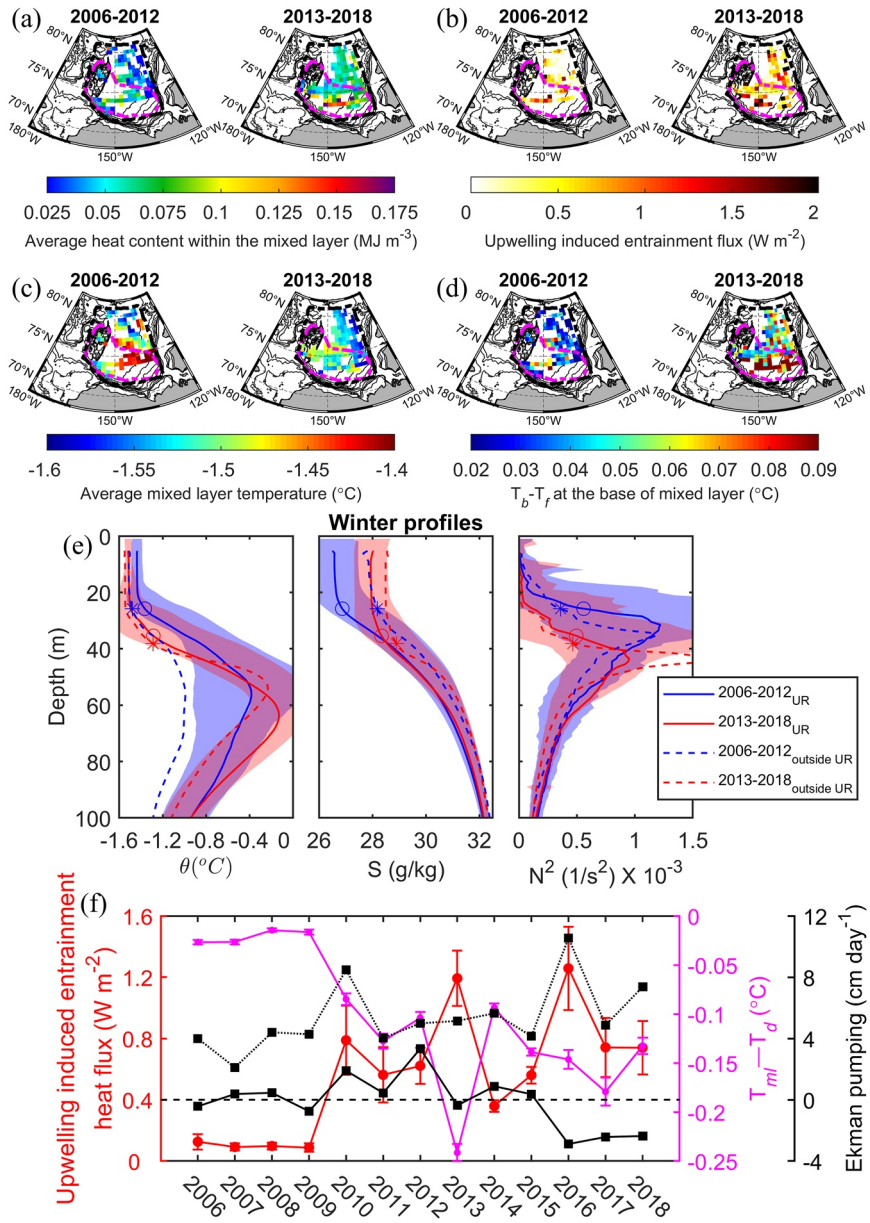

Figure 3. Winter (a) average heat content per meter within the mixed layer ($c_p \int_0^h \rho(T - T_f)dz/h$, where h is the mixed layer depth), (b) upwelling induced entrainment flux, (c) in-situ temperature at the depth of ~10 m, (d) in-situ temperature minus freezing point at the base of the mixed layer, (e) potential temperature profiles (left panel), salinity (middle panel), and buoyancy frequency (right panel) during 2006–2012 and 2013–2018. The solid color lines are the average profiles inside the upwelling region (UR) while the dashed color lines are those outside the upwelling region (outside UR). The blue and red shading are the standard deviation of the mean profiles inside the upwelling region for each time period. The mean mixed layer depth for the profiles inside the upwelling region (circles) and outside the upwelling region (asterisks) are shown. (f) Beaufort Gyre (BG) regional mean upwelling induced entrainment heat flux (red solid line), and the temperature difference between the average mixed layer temperature and the temperature just below the mixed layer base ($T_{ml} - T_d$, pink solid line). In order to reduce clutter, those buoy drift positions that only presented with Ekman upwelling (black dashed line) and Ekman pumping for all buoy drifted positions (black solid line) are plotted as median value. The error bars represent the standard errors.

3.3. The Consequences of Thinner Sea Ice and Larger Ice Lead Fractions in Winter

Sea ice thickness in the southern Canada Basin experienced a dramatic decrease over the past decades (Kwok, 2018). Here, we utilize the MIZMAS model to study the changes of sea ice properties in winter over

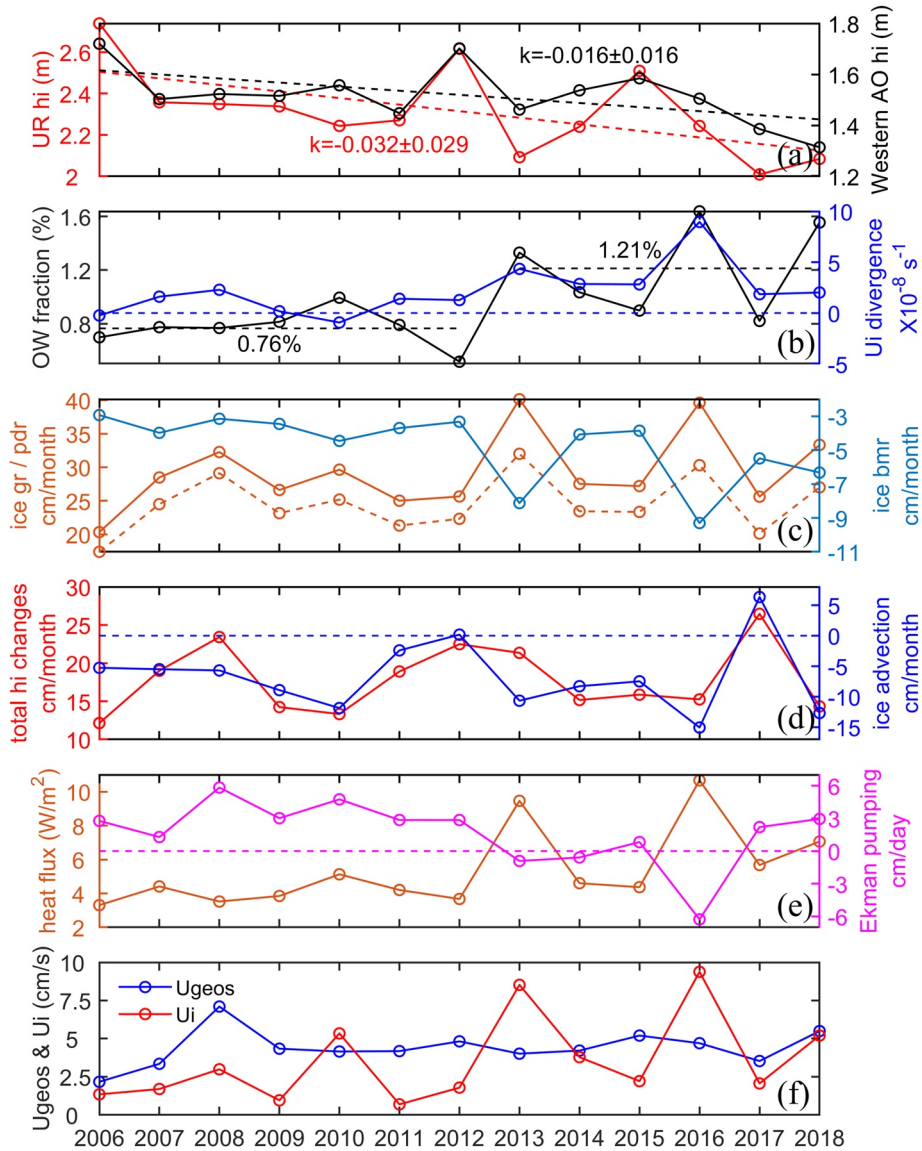

Figure 4. Marginal Ice Zone Modeling and Assimilation System (MIZMAS) model results in winter (averaged in the upwelling region) over 2006–2018, (a) Sea ice thickness averaged in the upwelling region (red line) versus that averaged in the western Arctic Ocean (black line), with "k" denoting the linear fit slope. (b) Open water (or lead) fractions (black line) versus ice divergence (blue line). (c) Ice growth rate (denoted as "ice gr" in the left *Y* axis, solid dots line) and ice production rate (denoted as "pdr" in the left *Y* axis, dashed dots line) versus ice melt rate (denoted as "ice bmr" in the right *Y* axis). The ice production rate here is equal to the ice growth rate plus ice melt rate. (d) Total changes in ice thickness (red line) versus the changes due to ice advection (blue line). (e) Model output of ocean surface net heat flux (here positive value indicates the ocean is losing heat, converted from the original model negative value to positive to compare with Figure 2b). The pink line represents the Ekman pumping velocity. (f) Ocean surface geostrophic current (Ugeos, blue line) versus sea ice velocity (Ui, red line).

2006–2018 (Figures 4 and S7 in Supporting Information S1). Results show winter ice thickness declined rapidly by −3.2 ± 2.9 cm/year over 2006–2018 in the upwelling region (Figures 4a and S7b in Supporting Information S1, because of extreme summer melt). This thinner ice tends to promote a stronger ice divergence and hence larger open water (or ice leads) fraction in later years (Figures 4b and S7d in Supporting Information S1). Both the thinner ice and increases in open waters would lead to an increase of ice production rate in the later period (Figures 4c and S7c in Supporting Information S1). The increased ice production rate tends to reject more brine water and trigger stronger ocean vertical convection. This in turn increases the upward entrainment of subsurface heat and thus enhances OHF (Figure 2) and leads to a cooler mixed layer in the later period (e.g., Figures 3c

and 3e). Stronger ice advection out of the region also contributes to larger open water fraction (Figure 4d) and thus larger ocean surface net heat flux (Figures 4e and S7a in Supporting Information S1). The model also shows reduction of Ekman upwelling in consistent with the changes of velocity difference between ice velocity and ocean current (Figures 4e and 4f). A caveat is that MIZMAS resolves only wide ice leads. Using a higher resolution version would more precisely reproduce the ice lead fractions and ice deformation rate (Zhang, 2021b), but would not change the general trend of lead fractions here. Model output of ocean surface net heat flux reveals a general increasing trend consistent with the estimated OHF (Figures 4e and 2b). Similar maxima of ocean heat loss in years 2013 and 2016 can be seen from both model and observations. This indicates the loss of buoyancy at the ocean surface which would trigger stronger vertical convection.

What is the effect of stronger winter ice growth and brine rejection on mixed layer salinity? Utilizing the model results, we estimate the corresponding salt production in kilograms per square meter per month as given by Cavalieri and Martin (1994) to consider the effect of larger ice lead fractions. Salt production is: $S_F = \rho_i V_i (s_w - s_i) 10^{-3}$, where ρ_i is the density of ice (900 kg/m^3), V_i is the ice production rate in units of m/month, S_w is the salinity of sea water, S_i is the salinity of frazil ice. The salinity of frazil ice is $s_i = 0.31 s_w$ according to the laboratory experiment by Martin and Kauffman (1981). Take the average profiles in summer for a diagnostic analysis, which the surface salinity increased from 25.8 to 26.5 g/kg (increase of 0.7 g/kg; Figure S6a in Supporting Information S1, middle panel). This is not enough to explain the observed winter mixed layer salinification with an increase of ~1.8 g/kg (the percentage of salt is 1.8×10^{-3}) in the upwelling region (e.g., Figure 3e, middle panels). However, the model results show the average ice production rate in the upwelling region increases from 23 cm/month during 2006–2012 to 26 cm/month during 2013–2018 (in some places the increases are larger). With a reference water density of 10^3 kg/m^3, the salt production of the winter mixed layer is estimated as 3.69 kg/month for 1 m^3 of water in 2006–2012. It increased to 4.28 kg/month for 1 m^3 of water in 2013–2018, with a total increase in salt of 1.77 kg for three winter months relative to 2006–2012 (the percentage of salt is 1.77×10^{-3}). This could explain the observed winter mixed layer salinification.

4. Conclusions and Discussion

Our results revealed that the winter ocean-to-ice heat flux increased from 0.76 ± 0.05 W/m^2 over 2006–2012 to 1.63 ± 0.08 W/m^2 over 2013–2018 in the BG region of the Arctic Ocean (an increase of 0.87 ± 0.09 W/m^2 between the two time periods). Larger OHF (>5 W/m^2) are more prevalent in the later years. The increased OHF resulted from an increase in $T_{7m} - T_f$ (mostly contributed by stronger convective entrainment) as well as parameterized ice-ocean shear u_* (shear entrainment) during winter months. However, its interannual variability is more strongly regulated by $T_{7m} - T_f$ than u_*. The increased heat flux resulted despite a decline in Ekman upwelling in later years, which supports the conclusion that upwelling plays a secondary role in increased heat fluxes. Such larger heat fluxes imply a larger entrainment of subsurface heat that we deduce results from (a) thinner ice with more ice leads that lead to more wintertime ice growth, (b) stronger ice motion, (c) stronger vertical convection, and (d) warmer subsurface water near the mixed layer base (potentially related with PSW). All of these processes are changing interannually in a way that will lead to increased OHF. An increase of 0.7 W/m^2 over the two periods will decrease ice growth by ~2 cm over January-March. Krishfield and Perovich (2005) revealed a positive trend of OHF over 1979–2002 with a parameterized $T_{7m} - T_f$ in which only the changes of sea ice velocity were responsible for the interannual variability. (Note that they also neglected the variability of surface geostrophic current.) Further (although different study periods), our results also revealed an interannual positive trend of winter $T_{7m} - T_f$, which suggests an increased entrainment of subsurface heat from beneath the mixed layer. While variations in stratification immediately beneath the mixed layer base are occurring (e.g., Figure 3e), any changes in stratification are apparently not sufficient to eliminate an increase of heat flux in winter.

The winter T-S profiles indicate that the mixed layer was cooler, saltier, and deeper over 2013–2018 relative to 2006–2012 (e.g., Figure 3e, left and middle panels); this change is even more pronounced in the upwelling regional average (~0.1 °C cooler and ~1.8 g/kg saltier in the later period). It is possible that this change may occur because of changes taking place in summer. Considering July-October over 2005–2011 and 2012–2017 (Figure S6 in Supporting Information S1), both the summer sea surface temperature (SST) and NSTM were cooler in 2012–2017 while the summer mixed layer was saltier. The more saline summer mixed layer (~0.7 g/kg) is not sufficient to explain the larger mixed layer salinity difference in winter in the upwelling region (but may be an effect

of the wintertime changes). We suggest that future studies consider the full seasonal and interannual variations to better understand how changes in one season can affect interannual trends.

One source of uncertainty in our results is the use of a constant ice-ocean drag coefficient, whereas observations exhibit a range of values of order 10^{-3} (e.g., Cole et al., 2017; Lu et al., 2011). How much of a change in the ice-ocean drag coefficient would need to have occurred for the OHF to be constant between the two periods? For basin median values to have remained at 0.26 W/m^2 instead of the estimated 0.49 W/m^2 (Figure 2c), C_{io} would have to have decreased by 16% during 2013–2018. This would correspond to $C_{io} = 5.5 \times 10^{-3}$ that decreased to $C_{io} = 4.6 \times 10^{-3}$, which is within the uncertainty of the observed C_{io}. C_{io} is related with the spatial variability of ice draft. While the PDF of ice thickness from both the model and Upward Looking Sonar data revealed a shift toward thinner ice thickness, the spatial variance hardly changed over the two periods (Figure S8 in Supporting Information S1) suggesting a stable wintertime ice-ocean drag coefficient. Seasonal variability can be safely neglected here as we consider only wintertime conditions. Recent observations (Brenner et al., 2021) also revealed little geographic variability in winter ice thickness and ice-ocean drag coefficient within the Beaufort Gyre. We can only speculate on potential interannual changes in C_{io} (increased due to more leads or increased ridging with thinner and more mobile ice cover; decreased due to thinner ice or smaller ridges), and so retain the constant C_{io} as the best approximation.

How the increased OHF should be interpreted depends in part on the timing of heat release from the NSTM. If wintertime OHF represents entrainment of PSW from beneath the halocline, the increased OHF could be illustrated as an increase in PSW entrainment. But if some of the NSTM heat in the summer surface layer is not released until the January-March time period due to a gradual deepening of the summer mixed layer (Figure S6a in Supporting Information S1), then the increased OHF could represent a change in the timing of this process, or a change in the heat input into the summer surface layer. Given the small values of OHF in winter and a cooler upper ocean in summers in the later period (Figures S6b and S6c in Supporting Information S1), it is most likely that the summer mixed layer heat is already entrained by the end of December, and so January-March heat fluxes represent heat entrained from PSW. In addition, we have not specifically determined the exact processes that could be involved in increased OHF during winter, including the role of mesoscale eddies that shoal the mixed layer base, submesoscale fronts that can restratify the mixed layer, or upwelling due to ice deformation. Such avenues are left for future studies.

Our results are somewhat sensitive to the buoy records that pass through the upwelling region. This area is a hot spot for subsurface heat release and favored by stronger entrainment heat flux. However, removing any one buoy record does not alter the general increasing trend of OHF, and this is a robust signal across multiple buoy systems. The key issues are the enhanced vertical temperature gradient along with the stronger convective entrainment. This vertical convection induced by larger ocean heat loss to the atmosphere would continue to entrain warmer PSW (Timmermans et al., 2018) heat upward which contributes to polar amplification (Beer et al., 2020). The ocean-to-ice heat fluxes will potentially continue to rise due to the ability to entrain warmer PSW in winter.

Data Availability Statement

The ship-based hydrographic data are provided by the Beaufort Gyre Exploration Project that maintained by the Woods Hole Oceanographic Institution (http://www.whoi.edu/website/beaufortgyre/), through the data tab on the website. The Ice-Tethered Profiler data were collected and made available by the Ice-Tethered Profiler Program based at the Woods Hole Oceanographic Institution (http://www.whoi.edu/itp), through the data products tab on the website. The Autonomous Ocean Flux Buoy (AOFB) data are obtained from https://www.oc.nps.edu/~stanton/fluxbuoy/index.html. The monthly Arctic Dynamic Ocean Topography data are distributed by CPOM and BAS (http://www.cpom.ucl.ac.uk/dynamic_topography/; https://doi.org/10.5285/cbd2cf78-462a-4968-be20-05f9c125ad10). The MIZMAS data are available from the Polar Sciences Center at the University of Washington (https://pscfiles.apl.uw.edu/zhang/MIZMAS168x180/).

Acknowledgments
This study was supported by the National Key Research and Development Program of China (2018YFA0605901), the National Natural Science Foundation of China (41941012; 42076225; 41776192; 41976219; 41706211). S. C. was supported by the Woods Hole Oceanographic Institution Early Career Scientist Fund and the Lenfest Fund for Early Career Scientists. J. Z. was supported by U.S. NSF Grants PLR-1603259, PLR-1602985, and NNA-1927785. M. S. was supported by U.S. ONR Grant N00014-17-1-2545, NSF Grants PLR 1603266 and OPP-1751363 and NOAA Grants NA15OAR4320063AM170 and NA20OAR4320271. W. Z. thanks Jiuxin Shi for discussion regarding the salt production, Xianyao Chen, Peigen Lin, and Min Li for help about statistical analysis. We thank Dr. Erica Rosenblum and the other three anonymous reviewers for their constructive comments.

References

Beer, E., Eisenman, I., & Wagner, T. J. W. (2020). Polar amplification due to enhanced heat flux across the halocline. *Geophysical Research Letters*, *47*, e2019GL086706. https://doi.org/10.1029/2019GL086706

Brenner, S., Rainville, L., Thomson, J., Cole, S., & Lee, C. (2021). Comparing observations and parameterizations of ice-ocean drag through an annual cycle across the Beaufort Sea. *Journal of Geophysical Research: Oceans*, *126*, e2020JC016977. https://doi.org/10.1029/2020JC016977

Cavalieri, D. J., & Martin, S. (1994). The contribution of Alaskan, Siberian, and Canadian coastal polynyas to the cold halocline layer of the Arctic Ocean. *Journal of Geophysical Research*, *99*(C9), 18343–18362. https://doi.org/10.1029/94JC01169

Cole, S. T., & Stadler, J. (2019). Deepening of the winter mixed layer in the Canada basin, Arctic Ocean over 2006–2017. *Journal of Geophysical Research: Oceans*, *124*, 4618–4630. https://doi.org/10.1029/2019JC014940

Cole, S. T., Toole, J. M., Lele, R., Timmermans, M.-L., Gallaher, S. G., Stanton, T. P., et al. (2017). Ice and ocean velocity in the Arctic marginal ice zone: Ice roughness and momentum transfer. *Elementa Science of the Anthropocene*, *5*, 55. https://doi.org/10.1525/elementa.241

Dewey, S., Morison, J., Kwok, R., Dickinson, S., Morison, D., & Andersen, R. (2018). Arctic ice-ocean coupling and gyre equilibration observed with remote sensing. *Geophysical Research Letters*, *45*, 1499–1508. https://doi.org/10.1002/2017GL076229

Fer, I., Peterson, A. K., Randelhoff, A., & Meyer, A. (2017). One-dimensional evolution of the upper water column in the Atlantic sector of the Arctic Ocean in winter. *Journal of Geophysical Research: Oceans*, *122*, 1665–1682. https://doi.org/10.1002/2016JC012431

Guthrie, J. D., & Morison, J. H. (2021). Not just sea ice: Other factors important to near-inertial wave generation in the Arctic Ocean. *Geophysical Research Letters*, *48*, e2020GL090508. https://doi.org/10.1029/2020GL090508

Guthrie, J. D., Morison, J. H., & Fer, I. (2013). Revisiting internal waves and mixing in the Arctic Ocean. *Journal of Geophysical Research: Oceans*, *118*, 3966–3977. https://doi.org/10.1002/jgrc.20294

Hibler, W. D. III (1979). A dynamic thermodynamic sea ice model. *Journal of Physical Oceanography*, *9*(4), 815–846. https://doi.org/10.1175/1520-0485(1979)009<0815:adtsim>2.0.co;2

Hibler, W. D., & Bryan, K. (1987). A diagnostic ice ocean model. *Journal of Physical Oceanography*, *17*, 987–1015. https://doi.org/10.1175/1520-0485(1987)017<0987:ADIM>2.0.CO;2

Jackson, J. M., Carmack, E. C., McLaughlin, F. A., Allen, S. E., & Ingram, R. G. (2010). Identification, characterization, and change of the near-surface temperature maximum in the Canada Basin, 1993–2008. *Journal of Geophysical Research*, *115*, C05021. https://doi.org/10.1029/2009JC005265

Jackson, J. M., Williams, W. J., & Carmack, E. C. (2012). Winter sea-ice melt in the Canada basin, Arctic Ocean. *Geophysical Research Letters*, *39*, L03603. https://doi.org/10.1029/2011GL050219

Krishfield, R., Toole, J., & Timmermans, M.-L. (2008). *ITP data processing procedures*. In *Woods Hole Oceanographic Institute* (Technical Report, Vol. 24). Retrieved from http://www.whoi.edu/fileserver.do?id=35803&pt=2&p=41486

Krishfield, R. A., & Perovich, D. K. (2005). Spatial and temporal variability of oceanic heat flux to the Arctic ice pack. *Journal of Geophysical Research*, *110*, C07021. https://doi.org/10.1029/2004JC002293

Krishfield, R. A., Proshutinsky, A., Tateyama, K., Williams, W. J., Carmack, E. C., McLaughlin, F. A., & Timmermans, M.-L. (2014). Deterioration of perennial sea ice in the Beaufort Gyre from 2003 to 2012 and its impact on the oceanic freshwater cycle. *Journal of Geophysical Research: Oceans*, *119*, 1271–1305. https://doi.org/10.1002/2013JC008999

Kwok, R. (2018). Arctic sea ice thickness, volume, and multiyear ice coverage: Losses and coupled variability (1958–2018). *Environmental Research Letters*, *13*(10), 105005. https://doi.org/10.1088/1748-9326/aae3ec

Kwok, R., & Rothrock, D. A. (2009). Decline in Arctic sea ice thickness from submarine and ICESat records: 1958–2008. *Geophysical Research Letters*, *36*, L15501. https://doi.org/10.1029/2009GL039035

Lei, R., Cheng, B., Heil, P., Vihma, T., Wang, J., Ji, Q., & Zhang, Z. (2018). Seasonal and interannual variations of sea ice mass balance from the Central Arctic to the Greenland Sea. *Journal of Geophysical Research: Oceans*, *123*, 2422–2439. https://doi.org/10.1002/2017JC013548

Lincoln, B. J., Rippeth, T. P., Lenn, Y.-D., Timmermans, M. L., Williams, W. J., & Bacon, S. (2016). Wind-driven mixing at intermediate depths in an ice-free Arctic Ocean. *Geophysical Research Letters*, *43*, 9749–9756. https://doi.org/10.1002/2016GL070454

Lu, P., Li, Z., Cheng, B., & Leppƒaranta, M. (2011). A parameterization of the ice-ocean drag coefficient. *Journal of Geophysical Research*, *116*, C07019. https://doi.org/10.1029/2010JC006878

Martin, S., & Kauffman, P. (1981). A field and laboratory study of wave dumping by grease ice. *Journal of Glaciology*, *27*(96), 283–313. https://doi.org/10.3189/s0022143000015392

Maykut, G., & McPhee, M. G. (1995). Solar heating of the Arctic mixed layer. *Journal of Geophysical Research*, *100*(C12), 24691–24703. https://doi.org/10.1029/95JC02554

Maykut, G. A. (1982). Large-scale heat exchange and ice production in the central Arctic. *Journal of Geophysical Research*, *87*(C10), 7971–7984. https://doi.org/10.1029/JC087iC10p07971

Maykut, G. A., & Untersteiner, N. (1971). Some results from a time-dependent thermodynamic model of sea ice. *Journal of Geophysical Research*, *76*(6), 1550–1575. https://doi.org/10.1029/JC076i006p01550

McPhee, M. G. (1975). Ice-momentum transfer for the AIDJEX ice model. *AIDJEX Bulletin*, *29*, 93–112.

McPhee, M. G. (1992). Turbulent heat flux in the upper ocean under sea ice. *Journal of Geophysical Research*, *97*(C4), 5365–5379. https://doi.org/10.1029/92JC00239

McPhee, M. G., Kikuchi, T., Morison, J. H., & Stanton, T. P. (2003). Ocean-to-ice heat flux at the North Pole environmental observatory. *Geophysical Research Letters*, *30*(24), 2274. https://doi.org/10.1029/2003GL018580

Meneghello, G., Marshall, J., Lique, C., Isachsen, P. E., Doddridge, E., Campin, J.-M., et al. (2020). Genesis and decay of mesoscale baroclinic eddies in the seasonally ice-covered interior Arctic Ocean. *Journal of Physical Oceanography*, *51*(1), 115–129. https://doi.org/10.1175/JPO-D-20-0054.1

Meneghello, G., Marshall, J., Timmermans, M., & Scott, J. (2018). Observations of seasonal upwelling and downwelling in the Beaufort Sea mediated by sea ice. *Journal of Physical Oceanography*, *48*(4), 795–805. https://doi.org/10.1175/JPO-D-17-0188.1

Peralta-Ferriz, C., & Woodgate, R. A. (2015). Seasonal and interannual variability of pan-Arctic surface mixed layer properties from 1979 to 2012 from hydrographic data, and the dominance of stratification for multiyear mixed layer depth shoaling. *Progress in Oceanography*, *134*, 19–53. https://doi.org/10.1016/j.pocean.2014.12.005

Peterson, A. K., Fer, I., McPhee, M. G., & Randelhoff, A. (2017). Turbulent heat and momentum fluxes in the upper ocean under Arctic sea ice. *Journal of Geophysical Research: Oceans*, *122*, 1439–1456. https://doi.org/10.1002/2016JC012283

Petty, A. A., Holland, M. M., Bailey, D. A., & Kurtz, N. T. (2018). Warm Arctic, increased winter sea ice growth? *Geophysical Research Letters*, *45*, 12922–12930. https://doi.org/10.1029/2018GL079223

Planck, C. J., Perovich, D. K., & Light, B. (2020). A synthesis of observations and models to assess the time series of sea ice mass balance in the Beaufort Sea. *Journal of Geophysical Research: Oceans*, *125*, e2019JC015833. https://doi.org/10.1029/2019JC015833

Polyakov, I. V., Pnyushkov, A. V., Rember, R., Padman, L., Carmack, E. C., & Jackson, J. M. (2013). Winter convection transports Atlantic water heat to the surface layer in the eastern Arctic Ocean. *Journal of Physical Oceanography*, *43*, 2142–2155. https://doi.org/10.1175/jpo-d-12-0169.1

Polyakov, I. V., Rippeth, T. P., Fer, I., Alkire, M. B., Baumann, T. M., Carmack, E. C., et al. (2020). Weakening of cold halocline layer exposes sea ice to oceanic heat in the eastern Arctic Ocean. *Journal of Climate*, *33*(18), 8107–8123. https://doi.org/10.1175/jcli-d-19-0976.1

Shaw, W. J., Stanton, T. P., McPhee, M. G., & Kikuchi, T. (2008). Estimates of surface roughness length in heterogeneous under-ice boundary layers. *Journal of Geophysical Research*, *113*, C08030. https://doi.org/10.1029/2007JC004550

Steele, M., Ermold, W., & Zhang, J. (2011). Modeling the formation and fate of the near-surface temperature maximum in the Canadian Basin of the Arctic Ocean. *Journal of Geophysical Research*, *116*, C11015. https://doi.org/10.1029/2010JC006803

Steele, M., & Morison, J. H. (1993). Hydrography and vertical fluxes of heat and salt northeast of Svalbaard in autumn. *Journal of Geophysical Research*, *98*(C6), 10013–10024. https://doi.org/10.1029/93JC00937

Steele, M., Zhang, J., & Ermold, W. (2010). Mechanisms of summertime upper Arctic Ocean warming and the effect on sea ice melt. *Journal of Geophysical Research*, *115*, C11004. https://doi.org/10.1029/2009JC005849

Stevenson, J. W., & Niiler, P. P. (1983). Upper ocean heat budget during the Hawaii-to-Tahiti shuttle experiment. *Journal of Physical Oceanography*, *13*(10), 1894–1907. https://doi.org/10.1175/1520-0485(1983)013<1894:UOHBDT>2.0.CO;2

Timmermans, M.-L. (2015). The impact of stored solar heat on Arctic sea ice growth. *Geophysical Research Letters*, *42*, 6399–6406. https://doi.org/10.1002/2015GL064541

Timmermans, M.-L., Toole, J., & Krishfield, R. (2018). Warming of the interior Arctic Ocean linked to sea ice losses at the basin margins. *Science Advances*, *4*(8), 6773. https://doi.org/10.1126/sciadv.aat6773

Toole, J. M., Timmermans, M.-L., Perovich, D. K., Krishfield, R. A., Proshutinsky, A., & Richter-Menge, J. A. (2010). Influences of the ocean surface mixed layer and thermohaline stratification on Arctic sea ice in the central Canada Basin. *Journal of Geophysical Research*, *115*, C10018. https://doi.org/10.1029/2009JC005660

Wang, Q., Marshall, J., Scott, J., Meneghello, G., Danilov, S., & Jung, T. (2019). On the feedback of ice-ocean stress coupling from geostrophic currents in an anticyclonic wind regime over the Beaufort Gyre. *Journal of Physical Oceanography*, *49*(2), 369–383. https://doi.org/10.1175/jpo-d-18-0185.1

Yang, J., Comiso, J., Krishfield, R., & Honjo, S. (2001). Synoptic storms and the development of the 1997 warming and freshening event in the Beaufort Sea. *Geophysical Research Letters*, *28*(5), 799–802. https://doi.org/10.1029/2000GL011896

Zhang, J. (2021a). Sea ice properties in high-resolution sea ice models. *Journal of Geophysical Research: Oceans*, *126*, e2020JC016686. https://doi.org/10.1029/2020JC016686

Zhang, J. (2021b). Recent slowdown in the decline of Arctic sea ice volume under increasingly warm atmospheric and oceanic conditions. *Geophysical Research Letters*, *48*, e2021GL094780. https://doi.org/10.1029/2021GL094780

Zhang, J., Ashjian, C., Campbell, R., Spitz, Y. H., Steele, M., & Hill, V. (2015). The influence of sea ice and snow cover and nutrient availability on the formation of massive under-ice phytoplankton blooms in the Chukchi Sea. *Deep Sea Research Part II: Topical Studies in Oceanography*, *118*, 122–135. https://doi.org/10.1016/j.dsr2.2015.02.008

Zhang, J., Lindsay, R., Schweiger, A., & Rigor, I. (2012). Recent changes in the dynamic properties of declining Arctic sea ice: A model study. *Geophysical Research Letters*, *39*, L20503. https://doi.org/10.1029/2012GL053545

Zhang, J., Steele, M., Runciman, K., Dewey, S., Morison, J., Lee, C., et al. (2016). The Beaufort Gyre intensification and stabilization: A model-observation synthesis. *Journal of Geophysical Research: Oceans*, *121*, 7933–7952. https://doi.org/10.1002/2016JC012196

Zhong, W., Steele, M., Zhang, J., & Zhao, J. (2018). Greater role of geostrophic currents in Ekman dynamics in the western Arctic Ocean as a mechanism for Beaufort Gyre stabilization. *Journal of Geophysical Research: Oceans*, *123*, 149–165. https://doi.org/10.1002/2017JC013282

References From the Supporting Information

Armitage, T. W. K., Bacon, S., Ridout, A. L., Petty, A. A., Wolbach, S., & Tsamados, M. (2017). Arctic Ocean surface geostrophic circulation 2003-2014. *The Cryosphere*, *11*, 1767–1780. https://doi.org/10.5194/tc-11-1767-2017

Comiso, J. C. (2000). *Bootstrap sea ice concentrations from Nimbus-7 SMMR and DMSP SSM/I-SSMIS, version 2 [Northern Hemisphere/daily]*. NASA National Snow and Ice Data Center Distributed Active Archive Center. https://doi.org/10.5067/J6JQLS9EJ5HU

Kalnay, E., Kanamitsu, M., Kistler, R., Collins, W., Deaven, D., Gandin, L., et al. (1996). The NCEP/NCAR 40-year reanalysis project. *Bulletin of the American Meteorological Society*, *77*, 437–471. https://doi.org/10.1175/1520-0477(1996)077<0437:tnyrp>2.0.co;2

Landy, J., & Stroeve, J. (2020). Arctic sea ice and physical oceanography derived from CryoSat-2 Baseline-C Level 1b waveform observations, Oct-Apr 2010-2018 [Dataset]. UK Polar Data Centre, Natural Environment Research Council, UK Research & Innovation. https://doi.org/10.5285/cbd2cf78-462a-4968-be20-05f9c125ad10

Nguyen, A. T., Menemenlis, D., & Kwok, R. (2011). Arctic ice-ocean simulation with optimized model parameters: Approach and assessment. *Journal of Geophysical Research*, *116*, C04025. https://doi.org/10.1029/2010JC006573

Smith, R. D., Dukowicz, J. K., & Malone, R. C. (1992). Parallel ocean general circulation modeling. *Physica D*, *60*, 38–61. https://doi.org/10.1016/0167-2789(92)90225-c

Tschudi, M., Meier, W. N., Stewart, J. S., Fowler, C., & Maslanik, J. (2019). *Polar Pathfinder daily 25 km EASE-grid sea ice motion vectors, version 4*. NASA National Snow and Ice Data Center Distributed Active Archive Center. https://doi.org/10.5067/INAWUWO7QH7B

Zhang, J., & Steele, M. (2007). The effect of vertical mixing on the Atlantic water layer circulation in the Arctic Ocean. *Journal of Geophysical Research*, *112*, C04S04. https://doi.org/10.1029/2006JC003732

Zhong, W., Steele, M., Zhang, J., & Cole, S. T. (2019). Circulation of Pacific winter water in the western Arctic Ocean. *Journal of Geophysical Research: Oceans*, *124*, 863–881. https://doi.org/10.1029/2018JC014604